Implementation of a Walsh-Hadamard Gate in a Superconducting Qutrit

M. A. Yurtalan,[1,2,3,*] J. Shi[1,2] M. Kononenko[1,2] A. Lupascu,[1,2,4,†] and S. Ashhab[5]

[1]*Institute for Quantum Computing, University of Waterloo, Waterloo, Ontario N2L 3G1, Canada*
[2]*Department of Physics and Astronomy, University of Waterloo, Waterloo, Ontario N2L 3G1, Canada*
[3]*Department of Electrical and Computer Engineering, University of Waterloo, Waterloo, Ontario N2L 3G1, Canada*
[4]*Waterloo Institute for Nanotechnology, University of Waterloo, Waterloo, Ontario N2L 3G1, Canada*
[5]*Qatar Environment and Energy Research Institute, Hamad Bin Khalifa University, Qatar Foundation, Qatar*

We have implemented a Walsh-Hadamard gate, which performs a quantum Fourier transform, in a superconducting qutrit. The qutrit is encoded in the lowest three energy levels of a capacitively shunted flux device, operated at the optimal flux-symmetry point. We use an efficient decomposition of the Walsh-Hadamard gate into two unitaries, generated by off-diagonal and diagonal Hamiltonians, respectively. The gate implementation utilizes simultaneous driving of all three transitions between the three pairs of energy levels of the qutrit, one of which is implemented with a two-photon process. The gate has a duration of 35 ns and an average fidelity over a representative set of states, including preparation and tomography errors, of 99.2%, characterized with quantum-state tomography. Compensation of ac-Stark and Bloch-Siegert shifts is essential for reaching high gate fidelities.

In recent years, significant progress has been made toward the implementation of quantum computers. Current efforts are mainly focused on encoding quantum information using two-state systems, or qubits. Using multilevel systems, or qudits, instead of qubits to perform quantum information processing is a developing field that promises advantages in a number of areas of quantum information. Universal quantum control of qudits and quantum error correction approaches have been explored theoretically [1–3]. Recent theoretical work suggests that quantum error correction with qudits has potential advantages over qubit-based schemes [4–7]. The experimental implementation of quantum computing based on qudits is still largely unexplored. Besides quantum computing, qudits have been explored as alternatives to qubits in other areas of quantum information, as an improved platform for quantum metrology [8] and quantum communication [9].

In this Letter, we report the implementation of the generalized Walsh-Hadamard gate in a superconducting three-state qudit, or qutrit. The Walsh-Hadamard gate is one of the elementary gates in qudit control, relevant for error correction [1,2] and the implementation of the quantum Fourier transform in single- and many-qudit systems [10]. We use a fast single-pulse implementation of the gate based on a single rotation in the qutrit space. We note that superconducting devices provide a natural platform for the exploration of the physics of qutrits, with work to date including basic control and tomography [11], emulation of spin dynamics [12] and topological states of matter [13], the use of the third level of a qutrit to facilitate two-qubit gates [14], wave mixing [15], holonomic gates

[16], electromagnetic induced transparency [17], demonstration of quantum contextuality [18], and adiabatic state transfer protocols [19].

There have been several studies in the literature on decomposing qudit gates into sequences of simple steps, e.g., into a sequence of gates that each operates on two quantum states [20–22]. In this work we implement the Walsh-Hadamard gate for a qutrit, given by

$$U_{\mathrm{WH}} = \frac{1}{\sqrt{3}} \begin{pmatrix} 1 & 1 & 1 \\ 1 & e^{i(2\pi/3)} & e^{-i(2\pi/3)} \\ 1 & e^{-i(2\pi/3)} & e^{i(2\pi/3)} \end{pmatrix}, \quad (1)$$

using a decomposition that only requires two steps. Specifically, $U_{\mathrm{WH}} = U_d U_o$, with $U_o = \exp(-iG_o t)$ and $U_d = \exp(-iG_d t)$. The generators $G_o = (\sum_{0 \le j < k \le 2} m_{jk} |j\rangle\langle k|) + \mathrm{H.c.}$ and $G_d = \mathrm{diag}(\phi_0, \phi_1, \phi_2)$. We note that there are multiple distinct decompositions of this type with different values of the complex numbers m_{01}, m_{02}, and m_{12} and real numbers ϕ_0, ϕ_1, and ϕ_2 and we chose the decomposition that results in the shortest pulse duration for a given drive amplitude. This type of decomposition is well suited for superconducting circuits where microwave-based control allows for the application of broadband signals containing multiple frequency tones that can simultaneously drive transitions between different levels, allowing to readily implement G_o. The effect of the diagonal unitary U_d can be implemented without applying any additional pulses, but rather by shifting the phases of the drive fields in the next resonant control
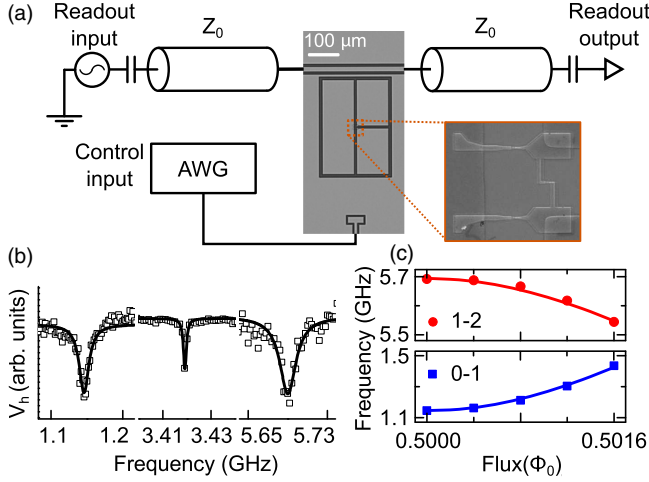
FIG. 1. (a) Schematic and microscope images of the device used in the experiment. The device is coupled to a coplanar waveguide resonator with characteristic impedance Z_0 for readout and a drive pad for control with pulses generated by an arbitrary waveform generator. The inset shows the magnified view of the device junctions and the loop. (b) Readout homodyne voltage V_h versus the frequency of the spectroscopy tone applied to the qutrit at the flux-symmetry point, showing the 0–1, two-photon 0–2, and 1–2 transitions, respectively. The solid lines represent Lorentzian fits. (c) Peak positions for the 0–1 (blue squares) and 1–2 (red dots) transitions versus applied magnetic flux. The solid lines represent the fits with the circuit model based on the calculated qutrit energies.

pulses. In our experiment, these phase shifts are applied to the tomography pulses. We note that a decomposition of qutrit gates based on a single pulse with detuned tones was proposed in Ref. [23]. Simultaneous driving of three-state subspaces in superconducting devices was applied to quantum emulation [13] and adiabatic transfer protocols [19].

The device used in our experiments, shown in Fig. 1(a), is formed of a superconducting loop with three Josephson junctions and three large capacitor pads. The device is capacitively coupled to a coplanar waveguide half-wavelength resonator for dispersive readout and to a transmission line terminated by a capacitor pad for control [24]. Similar devices, based on three Josephson junction loops with capacitive shunts, were employed as qubits encoded in the lowest two energy levels [25–27]. We employ control pulses generated using direct synthesis by a fast arbitrary waveform generator, model Tektronix TEK70001A, with a sampling rate of 50 GS/s. The pulses consist of single- and multitone signals with an envelope that has cosine shape rise and fall parts and a flattop. The device loop is biased with a magnetic flux generated by external superconducting coils. The device is placed inside a sample holder at the mixing chamber of a dilution refrigerator at 27 mK. All transmission lines contain attenuators, microwave low-pass filters and infrared filters.

We first perform spectroscopy measurements to characterize the qutrit. Figure 1(b) shows the results of spectroscopy of the device at the flux-symmetry point $\Phi = \Phi_0/2$. We identify the 0–1 and 1–2 transitions at frequencies $\omega_{01} = 2\pi \times 1.146$ GHz and $\omega_{12} = 2\pi \times 5.693$ GHz, respectively. The 0–2 transition, which is forbidden at the symmetry point, is visible as a two-photon excitation process at frequency $\omega_{02}^{2p} = 2\pi \times 3.420$ GHz. The 0–1 and 1–2 transition peak widths change linearly with driving amplitude whereas the 0–2 peak width has a quadratic dependence on the applied driving amplitude, as expected for one and two photon processes respectively. Figure 1(c) shows the flux dependence of the 0–1 and 1–2 transition frequencies. The spectroscopy data is in excellent agreement with calculations based on a circuit model (see Supplemental Material [31]) where the capacitance matrix is extracted from electromagnetic simulations and the junction critical currents are slightly adjusted with respect to nominal microfabrication values to fit the data.

Next, we discuss the qutrit thermal-state populations and implementation of qutrit state tomography. The thermal-state occupation probabilities P_{th0} and P_{th1} for states 0 and 1 are determined by comparing the amplitudes of the Rabi oscillations in the 0–1 transition with two different initial states: the qutrit thermal state with populations of states 1 and 2 swapped, and the thermal state with the populations of states 0 and 2 swapped [24]. Here, we ignore the thermal-state population P_{th2} of state 2, which gives a good approximation for P_{th0} and P_{th1} given that the temperature is low relative to the frequency of the 1–2 transition. The average thermal-state population in the ground state is $P_{th0} = 0.74 \pm 0.01$. State measurement is done using dispersive readout [11,28]. The average homodyne voltage $V_h = P_0 V_{h0} + P_1 V_{h1} + P_2 V_{h2}$, where V_{h0}, V_{h1}, and V_{h2} are average voltages corresponding to the three qutrit states and P_0, P_1, and P_2 are the occupation probabilities of the qutrit states immediately prior to the measurement. The experimental procedure used to determine the voltage levels V_{h0}, V_{h1}, and V_{h2} is given in the Supplemental Material [31].

To reconstruct the density matrix ρ of the qutrit state, we use a quantum-state tomography procedure in which the homodyne voltage is measured following the application of each pulse from a set of nine tomography pulses (see Table I). The tomography pulses are designed to optimize the readout by utilizing the large difference between V_{h1} and V_{h0}; this set of pulses is different from those used in the experiment of Bianchetti *et al.* [11], where contrast is maximum between states 1 and 2. The tomography pulses consist of combinations of rotations, denoted by $R_\alpha^{01(12)}(\theta)$, where $\alpha = x, y$ is the rotation axis and θ is the rotation angle.

The implementation of the Walsh-Hadamard gate discussed above requires the simultaneous driving of all three qutrit transitions such that the effective Hamiltonian in the rotating frame has nonzero values for all off-diagonal

TABLE I. Set of pulses used in state preparation and state tomography experiments.

State prep.	Rotations	Tomography pulses	Rotations
p_0	I	u_0	$R_x^{01}(\pi)$
p_1	$R_x^{01}(\pi)$	u_1	$R_x^{01}(\pi/2)$
p_2	$R_x^{12}(\pi)R_x^{01}(\pi)$	u_2	$R_y^{01}(\pi/2)$
p_3	$R_x^{01}(\pi/2)$	u_3	I
p_4	$R_y^{01}(\pi/2)$	u_4	$R_x^{12}(\pi/2)R_x^{01}(\pi)$
p_5	$R_x^{12}(\pi/2)R_x^{01}(\pi)$	u_5	$R_y^{12}(\pi/2)R_x^{01}(\pi)$
p_6	$R_y^{12}(\pi/2)R_x^{01}(\pi)$	u_6	$R_x^{01}(\pi)R_x^{12}(\pi/2)R_x^{01}(\pi)$
p_7	$R_x^{12}(\pi)R_x^{01}(\pi/2)$	u_7	$R_x^{01}(\pi)R_y^{12}(\pi/2)R_x^{01}(\pi)$
p_8	$R_x^{12}(\pi)R_y^{01}(\pi/2)$	u_8	$R_x^{01}(\pi)R_x^{12}(\pi)R_x^{01}(\pi)$

matrix elements. While the 0–1 and 1–2 transitions are allowed and can be implemented by standard resonant driving, the 0–2 transition is forbidden at the symmetry point, and is therefore implemented as a two-photon process. Figure 2(a) shows the Rabi frequency of the two-photon oscillations between states 0 and 2 versus the detuning $\delta_{02}^{2p} = (\omega_{01} + \omega_{12})/2 - \omega_{d,02}^{2p}$, where $\omega_{d,02}^{2p}$ is the driving frequency. The resonant Rabi oscillations have a minimum frequency of $2\pi \times 7.2$ MHz at a detuning $\delta_{02}^{2p} = -2\pi \times 3.5$ MHz. The fact that the resonance for the Rabi oscillations occurs at a nonvanishing detuning is due to fact that the strong field of 0–2 two-photon drive induces non-negligible ac-Stark and Bloch-Siegert shifts on
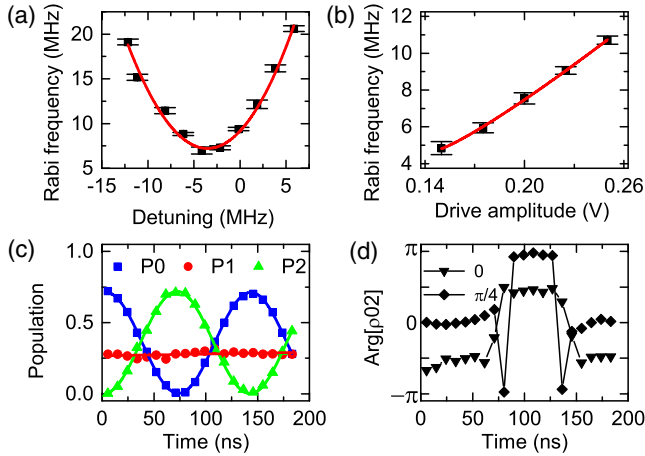

FIG. 2. Two-photon driving experiments. (a) Frequency of the Rabi oscillations versus the detuning between the driving frequency and the two-photon resonance frequency ($\omega_{01} + \omega_{12}$)/2 for a given drive amplitude. The line is a quadratic fit. (b) Two-photon resonant-driving Rabi frequency versus drive amplitude. The line is a quadratic fit. (c),(d) Results of the tomography experiments. Panel (c) shows the population of states 0 (blue squares), 1 (red disks), and 2 (green triangles), versus Rabi pulse duration, with an oscillation frequency of $2\pi \times 7.2$ MHz. Panel (d) shows the phase of the 0–2 component of the density matrix for two values of the phase of the driving field: 0 (triangles) and $\pi/4$ (rhombuses).

the energy levels. On resonance, the frequency of the Rabi oscillations depends quadratically on the drive amplitude [Fig. 2(b)], characteristic of a two-photon process. We performed tomography experiments for various durations of the 0–2 Rabi pulse, as shown in Figs. 2(c) and 2(d). The population oscillates between states 0 and 2, while the population of state 1 remains relatively constant at the level of the thermal state. The argument of the $\langle 0|\rho|2\rangle$ element of the density matrix ρ, shown in Fig. 2(d), is constant during each half-oscillation period, indicating rotation around a constant axis in the $\{|0\rangle, |2\rangle\}$ subspace. The two data sets in Fig. 2(d) correspond to two values of the phase of the two-photon driving tone, different by $\pi/4$. The phase of $\langle 0|\rho|2\rangle$ changes by twice the driving tone phase, which is another indication that the transition is a two-photon process. The results of the two-photon driving tomography experiment agree with numerical simulations based on the multilevel Hamiltonian, with the amplitude of the driving voltage at the qutrit being the only adjustable parameter. We note that in the numerical simulations we only obtained good agreement when taking into account at least the lowest seven energy levels, underscoring the importance of ac-Stark and Bloch-Siegert shifts in the experiment.

We next present the characterization of the Walsh-Hadamard gate. We use a decomposition where the off-diagonal generator has coefficients $m_{01} = 0.3491 + 0.6046i$, $m_{12} = -0.6981$, and $m_{02} = 0.3491 + 0.6046i$ and the diagonal generator has elements $\phi_0 = 6.1086$, $\phi_1 = 4.0143$, and $\phi_2 = 4.0143$. As mentioned above, the off-diagonal Hamiltonian that generates U_o is obtained by the simultaneous driving of the transitions 0–1, 1–2, and 0–2, with the latter being a two-photon process. The Rabi frequencies are $\tilde{\Omega}_{01} = \tilde{\Omega}_{12} = \tilde{\Omega}_{02} = 2\pi \times 7.2$ MHz. The Rabi frequencies are all equal because $|m_{01}| = |m_{02}| = |m_{12}|$, and they are maximized within the available voltage range of our pulse generation setup. We note that the control signal amplitude is not limited by the qutrit properties and larger driving amplitudes could in principle be reached by increasing signal transmission and the coupling to the capacitive driving line. During the control pulse, the drive frequencies are dynamically adjusted to match the transition frequency with ac-Stark and Bloch-Siegert shifts included, with the latter dependent on the driving amplitude (see Supplemental Material [31]).

The frequency shift of the 0–1 transition, which includes contributions from the ac-Stark and Bloch-Siegert shifts, is experimentally determined as follows. A driving field is applied with a detuning of $2\pi \times 50$ MHz from the 0–2 two-photon resonance. This detuning is chosen to be much larger than the strength of the two-photon process (when applied on resonance). Therefore, transitions between the 0 and 2 states are negligible, while the ac-Stark and Bloch-Siegert shifts are almost the same as those induced in the case of resonant driving. The shifts can then be measured

(a)

(b) Re(ρ)
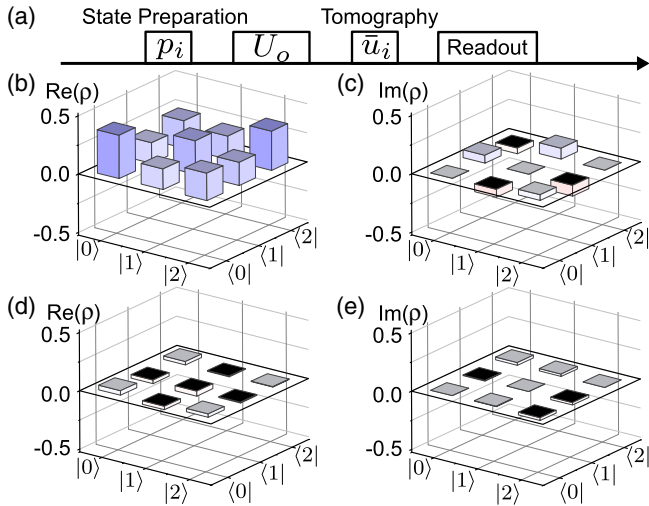
(c) Im(ρ)

(d) Re(ρ)

(e) Im(ρ)

FIG. 3. (a) Pulse sequence used in the experiments. (b) Real and (c) imaginary parts of the reconstructed density matrix after the gate is applied on the thermalized state shows a 99.8% gate fidelity. The differences between the reconstructed and the expected density matrices are shown for the real (d) and imaginary (e) parts.

directly by applying a microwave pulse to drive the 0–1 transition and measuring the induced Rabi oscillations. The driving frequency at which the Rabi oscillations have their minimum frequency is a direct measure of the resonance frequency, which includes the shifts caused by the strong 0–2 drive. The experimentally determined total shift of $2\pi \times 9.4$ MHz is in agreement with that obtained from numerical simulations.

The diagonal Hamiltonian that generates U_d is effectively embedded in the tomography pulses by shifting the phases of the driving fields for the latter. The new tomography analyzer pulses are given by $\bar{u}_i = U_d^\dagger u_i U_d$. The pulse sequence is shown in Fig. 3(a). The off-diagonal Hamiltonian is applied on the prepared states p_i followed by the phase-shifted tomography pulses $\bar{u}_i$ to complete the Walsh-Hadamard gate and to reconstruct the density matrix ρ of the state after the gate.

The gate fidelity is measured with respect to the ideal evolution of the prepared state under the gate Hamiltonian in Eq. (1). Figure 3 shows the real (b) and imaginary (c) elements of ρ where the gate is applied on the qutrit thermal state. The state fidelity after the gate in this case is 99.8%. The difference between the reconstructed and the expected density matrices are shown in Figs. 3(d) and 3(e) for the real and imaginary parts, respectively. Table II shows the fidelity values of the gate applied on nine different prepared states. On average over the nine preparations, the state fidelity at the end of the sequence is observed to be $99.2 \pm 0.1\%$. We estimate the error in the evolution by applying a maximum likelihood estimation procedure (see Supplemental Material [31]) together with the errors associated with the state homodyne voltage

TABLE II. Set of pulses used to prepare different states to which the Walsh-Hadamard gate is applied and measured fidelities.

State prep. (p_i)	Fidelity	State prep. (p_i)	Fidelity
I	99.8%	$R_x^{12}(\pi/2)\,R_x^{01}(\pi)$	98.7%
$R_x^{01}(\pi)$	99.8%	$R_y^{12}(\pi/2)\,R_x^{01}(\pi)$	98.3%
$R_x^{12}(\pi)\,R_x^{01}(\pi)$	98.8%	$R_x^{12}(\pi)\,R_x^{01}(\pi/2)$	99.6%
$R_x^{01}(\pi/2)$	99.8%	$R_x^{12}(\pi)\,R_y^{01}(\pi/2)$	98.5%
$R_y^{01}(\pi/2)$	99.6%		

levels. We also utilize quantum process tomography to quantify the process fidelity (see Supplemental Material [31]). The process fidelity of the Walsh-Hadamard gate is found to be 97.3%.

We next discuss numerical simulations of the evolution of the set of states obtained by applying the pulses listed in Table II to the qutrit steady state under the applied control pulse. The simulations are based on the system Hamiltonian with driving including the lowest seven energy levels of the system. The transition strengths are determined numerically with the circuit model including the complete capacitance matrix (see Supplemental Material [31]). The simulated fidelity of the off-diagonally generated part of the gate is 99.8% (99.7%) without (with) decoherence (see Supplemental Material [31]). To verify the role of the relative phase of the driving tones, we performed an experiment where the phase of the 0–2 two-photon driving tone was changed around its nominal value, based on the decomposition of the gate. Figure 4 shows the measured average fidelity of states after preparation by the pulses given in Table II and application of the Walsh-Hadamard gate versus the 0–2 two-photon drive phase. The data are in excellent agreement with the average fidelity values obtained from numerical simulations (dashed line in Fig. 4). We note that while the numerical simulations require the inclusion of several higher levels to accurately reproduce the experimentally observed driving strength and level shifts, the experimental implementation of the gate relies only on experimentally determined driving strengths and level shifts.
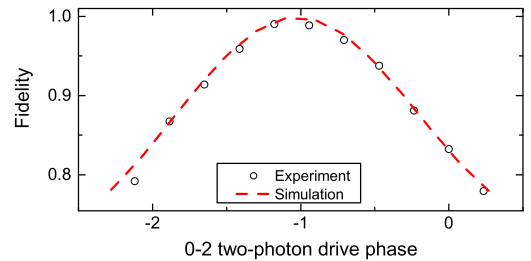

FIG. 4. Experimental (dots) and simulated (dashed curve) fidelity of the state obtained by applying the control pulse to the thermal state versus the relative phase of the 0–2 two-photon drive.

The results described above were obtained using the thermal state as the initial state. While this procedure did not pose a limitation for characterizing the qutrit gate, it is relevant to consider the possibility to prepare high purity initial states. To date, several initialization and state reset protocols have been demonstrated with superconducting qubits (see, e.g., [29,30]). In this work, we utilize a cooling technique based on a Raman process that effectively brings the qutrit 0–1 transition into resonance with the readout resonator. The fact that the resonator has a high resonance frequency and hence a small thermal excitation probability creates an effectively cold environment for the qutrit. By controlling the rate of transferring excitations between the qutrit and the resonator, the cooled qutrit state reaches a maximum ground-state probability of 0.94, a significant improvement over the probability of 0.74 in the thermal state. With the cooled state as the initial state for the Walsh-Hadamard gate, we measure an average state fidelity of 97.3% and a quantum process fidelity of 97.3%. While the process fidelity is identical within experimental errors for thermal state and cooling-based preparation, the average state fidelity is slightly lower in the latter case. This is possibly due to spurious excitation of the resonator having a reduced effect in combination with the strong state preparation pulses used in process tomography. The details and an extended analysis of the cooling process and quantum control on reset states are beyond the scope of the present work and will be addressed in future work.

In conclusion, we have implemented a Walsh-Hadamard gate in a superconducting qutrit. The implementation of the gate relied on a two-step decomposition, which only required the application of a single microwave pulse with three tones coupling the three pairs of qutrit energy levels. The experimentally characterized state fidelity after gate control is 99.2%, in agreement with the results of numerical simulations. We note that the ac-Stark and Bloch-Siegert shifts of the qutrit energy levels have to be accounted for in order to achieve a high fidelity gate. Our approach can be generalized to higher dimensionality qudits. This work demonstrates the potential of multitone multilevel control in superconducting devices and opens interesting avenues for exploration of superconducting qudits in quantum computing and other areas of quantum science.

[*]mayurtalan@uwaterloo.ca
[†]alupascu@uwaterloo.ca

[1] D. Gottesman, Chaos Solitons Fractals **10**, 1749 (1999).

[2] M. Grassl, M. Rötteler, and T. Beth, International Journal of Foundations of Computer Science **14**, 757 (2003).

[3] S. S. Bullock, D. P. OLeary, and G. K. Brennen, Phys. Rev. Lett. **94**, 230502 (2005).

[4] E. T. Campbell, H. Anwar, and D. E. Browne, Phys. Rev. X **2**, 041021 (2012).

[5] E. T. Campbell, Phys. Rev. Lett. **113**, 230501 (2014).

[6] H. Anwar, B. J. Brown, E. T. Campbell, and D. E. Browne, New J. Phys. **16**, 063038 (2014).

[7] A. Krishna and J.-P. Tillich, Phys. Rev. Lett. **123**, 070507 (2019).

[8] M. V. Suslov, G. B. Lesovik, and G. Blatter, Phys. Rev. A **83**, 052317 (2011).

[9] F. Bouchard, R. Fickler, R. W. Boyd, and E. Karimi, Sci. Adv. **3**, e1601915 (2017).

[10] A. Muthukrishnan and C. Stroud, J. Mod. Opt. **49**, 2115 (2002).

[11] R. Bianchetti, S. Filipp, M. Baur, J. M. Fink, C. Lang, L. Steffen, M. Boissonneault, A. Blais, and A. Wallraff, Phys. Rev. Lett. **105**, 223601 (2010).

[12] M. Neeley, M. Ansmann, R. C. Bialczak, M. Hofheinz, E. Lucero, A. D. O'Connell, D. Sank, H. Wang, J. Wenner, A. N. Cleland, M. R. Geller, and J. M. Martinis, Science **325**, 722 (2009).

[13] X. Tan, D.-W. Zhang, Q. Liu, G. Xue, H.-F. Yu, Y.-Q. Zhu, H. Yan, S.-L. Zhu, and Y. Yu, Phys. Rev. Lett. **120**, 130503 (2018).

[14] F. W. Strauch, P. R. Johnson, A. J. Dragt, C. J. Lobb, J. R. Anderson, and F. C. Wellstood, Phys. Rev. Lett. **91**, 167005 (2003).

[15] T. Hönigl-Decrinis, I. V. Antonov, R. Shaikhaidarov, V. N. Antonov, A. Y. Dmitriev, and O. V. Astafiev, Phys. Rev. A **98**, 041801(R) (2018).

[16] A. A. Abdumalikov Jr., J. M. Fink, K. Juliusson, M. Pechal, S. Berger, A. Wallraff, and S. Filipp, Nature (London) **496**, 482 (2013).

[17] A. A. Abdumalikov, O. Astafiev, A. M. Zagoskin, Y. A. Pashkin, Y. Nakamura, and J. S. Tsai, Phys. Rev. Lett. **104**, 193601 (2010).

[18] M. Jerger, Y. Reshitnyk, M. Oppliger, A. Potonik, M. Mondal, A. Wallraff, K. Goodenough, S. Wehner, K. Juliusson, N. K. Langford, and A. Fedorov, Nat. Commun. **7**, 12930 (2016).

[19] A. Vepsäläinen and G. S. Paraoanu, Adv. Quantum Technol. **3**, 1900121 (2020).

[20] N. V. Vitanov, Phys. Rev. A **85**, 032331 (2012).

[21] A. B. Klimov, R. Guzmán, J. C. Retamal, and C. Saavedra, Phys. Rev. A **67**, 062313 (2003).

[22] V. Ramakrishna, R. Ober, X. Sun, O. Steuernagel, J. Botina, and H. Rabitz, Phys. Rev. A **61**, 032106 (2000).

[23] A. R. Shlyakhov, V. V. Zemlyanov, M. V. Suslov, A. V. Lebedev, G. S. Paraoanu, G. B. Lesovik, and G. Blatter, Phys. Rev. A **97**, 022115 (2018).

[24] M. A. Yurtalan, J. Shi, G. J. K. Flatt, and A. Lupascu, arXiv:2008.00593.

[25] J. Q. You, X. Hu, S. Ashhab, and F. Nori, Phys. Rev. B **75**, 140515(R) (2007).

[26] M. Steffen, S. Kumar, D. P. DiVincenzo, J. R. Rozen, G. A. Keefe, M. B. Rothwell, and M. B. Ketchen, Phys. Rev. Lett. **105**, 100502 (2010).

[27] F. Yan, S. Gustavsson, A. Kamal, J. Birenbaum, A. P. Sears, D. Hover, T. J. Gudmundsen, D. Rosenberg, G. Samach, S. Weber, J. L. Yoder, T. P. Orlando, J. Clarke, A. J. Kerman, and W. D. Oliver, Nat. Commun. **7**, 12964 (2016).

[28] A. Wallraff, D. I. Schuster, A. Blais, L. Frunzio, J. Majer, M. H. Devoret, S. M. Girvin, and R. J. Schoelkopf, Phys. Rev. Lett. **95**, 060501 (2005).

[29] K. Geerlings, Z. Leghtas, I. M. Pop, S. Shankar, L. Frunzio, R. J. Schoelkopf, M. Mirrahimi, and M. H. Devoret, Phys. Rev. Lett. **110**, 120501 (2013).

[30] S. O. Valenzuela, W. D. Oliver, D. M. Berns, K. K. Berggren, L. S. Levitov, and T. P. Orlando, Science **314**, 1589 (2006).

[31] See Supplemental Material at http://link.aps.org/supplemental/10.1103/PhysRevLett.125.180504 for additional details on experimental techniques and theoretical modeling, which includes Refs. [32–34].

[32] G. Zizak, J. D. Bradshaw, and J. D. Winefordner, Appl. Opt. **19**, 3631 (1980).

[33] D. F. V. James, P. G. Kwiat, W. J. Munro, and A. G. White, Phys. Rev. A **64**, 052312 (2001).

[34] M. A. Nielsen and I. L. Chuang, *Quantum Computation and Quantum Information*, 10th ed. (Cambridge University Press, Cambridge, New York, 2010).